Biomimetic syntheses of pure or doped metal hydroxide nitrate thin films by a dual-template approach

Binbin Hu, Zhonghui Xue, Haiwei Wang, Li Cai, Haoyang Xiong, Xiaohong Jiang and Zuliang Du*

Received 29th September 2008, Accepted 20th January 2009
First published as an Advance Article on the web 23rd February 2009
DOI: 10.1039/b817003g

Compact large area $Zn_5(OH)_8(NO_3)_2 \cdot 2H_2O$, $Co_5(OH)_8(NO_3)_2 \cdot 2H_2O$ and Co-doped $Zn_5(OH)_8(NO_3)_2 \cdot 2H_2O$ thin films with uniform surface morphology and good orientation were synthesized by an unusual dual-template biomimetic approach. In such a biomimetic system, a bovine serum albumin Langmuir monolayer was used as one organic matrix template, whereas the vapor–liquid interface generated by the vapor diffusion of catalyst (ammonia) served as the other nucleation template providing kinetic control. The crystallinity, morphology and overall chemical composition of thin films were characterized by X-ray diffraction, scanning electron microscopy, transmission electron microscopy, and X-ray photoelectron spectroscopy. The formation process of the $Zn_5(OH)_8(NO_3)_2 \cdot 2H_2O$ films was discussed in detail. Compared with the method with only organic template, the synergetic effect of the dual template plays an important role in the formation of thin films. The method developed here provides a novel route for growing large area and well-oriented thin films at room temperature.

Introduction

Large area and well-oriented thin films have attracted extensive interest due to their widespread applications in liquid crystalline and photoelectric materials. Developing novel methods to grow compact large area thin films with controllable morphologies and superstructures is an ongoing research goal in crystal engineering owing to tremendous applications in the industrial processes.[1,2] Bio-inspired methods have been more and more considered as a promising way to synthesize lots of functional materials with special morphologies and crystal structures at room temperature.[3,4] It has been demonstrated that surfactant monolayers can be utilized as templates to nucleate and grow inorganic and organic crystals, and that geometrical and stereochemical matching of both monolayers and crystal lattices can result in oriented crystal growth along some planes.[5] Many kinds of materials, such as $CaCO_3$,[6–9] CaC_2O_4,[10] CdS[5] and $BaCO_3$,[11] have been fabricated in this way. However, such a biomimetic approach always results in well-oriented individual crystals rather than thin films primarily because of the limited nucleation sites provided by organic templates.

On the other hand, in recent years, increasing attention has been paid to inorganic layered solids formed by both hydroxides and hydroxy salts. These materials are viewed as useful substrates for designing advanced materials with a broad range of applications because of the ability to vary the interlayer cation and anion compositions.[12] Hitherto, the reported applications of such materials are chiefly focused on the preparation of anion exchangers, organic–inorganic hybrid materials, and slow release drug delivery agents.[13–17] Another important feature of such materials is that they can decompose under heating, allowing us to prepare simple oxides with unique sorptive, catalytic, magnetic or electric properties.[18] For example, hydroxy salts of zinc have been recently reported as exceptionally promising precursors of ZnO thin films with potential electronic and optoelectronic applications.[19,20] In 2006, nanostructured $Co_5(OH)_8Cl_2 \cdot 3H_2O$, $Co_5(OH)_8(NO_3)_2 \cdot 2H_2O$, $Co_5(OH)_8SO_4 \cdot 2H_2O$, $Cu_2(OH)_3(NO_3)$, $Zn_5(OH)_8(NO_3)_2 \cdot 2H_2O$, $Mn_3(PO_4)_2 \cdot 7H_2O$[21] and ZnO[22] thin films were prepared by Morse *et al.* using a kinetically controlled vapor-diffusion method.[21,22] In this method, vectorial control by diffusion of ammonia as a base catalyst into an aqueous metal salt solution yielded large area metal hydroxide films with unique structures. It should be noted that Morse *et al.*, for the first time, put forward the concept that the vapor–liquid interface generated by the vapor diffusion of catalyst (ammonia) can work as the nucleation template.[21] However, morphologies of the films obtained by the vapor–liquid interface template method are not very uniform; furthermore, their crystallographic orientation is random, the reason for which is the absence of organic matrix templates in the synthesis conditions. Additionally, as mentioned above, it has been proved that Langmuir monolayers as organic matrix templates can play a key role in controlling the morphology and crystallinity of the products in many biomimetic processes.[5–10] Considering the nucleation effect of the vapor–liquid interface template and the matrix role of the organic template, we think that the combination of both templates will construct uniform morphological and well-oriented thin films at ambient temperature. With this consideration in mind, we developed a combination strategy of the vapor–liquid interface nucleation template and the organic matrix template, which was named a dual-template approach. Our experimental results proved that this dual-template approach was rather effective in the preparations of uniform morphological and well-oriented thin films of pure or doped metal hydroxide nitrates. The most important characteristic of our developed

Key Lab for Special Functional Materials of Ministry of Education, Henan University, Kaifeng, 475004 P. R. China. E-mail: zld@henu.edu.cn; Fax: +86 378 3881358; Tel: +86 378 3881358

dual-template approach is the synergetic effect of the vapor–liquid interface nucleation template and the organic matrix template. In the present paper, we report the syntheses of compact large area $Zn_5(OH)_8(NO_3)_2\cdot 2H_2O$, $Co_5(OH)_8(NO_3)_2\cdot 2H_2O$ and Co-doped $Zn_5(OH)_8(NO_3)_2\cdot 2H_2O$ thin films with uniform surface morphology and good orientation along the (200) plane. They were characterized by X-ray diffraction (XRD), scanning electron microscopy (SEM), transmission electron microscopy (TEM), and X-ray photoelectron spectroscopy (XPS). Moreover, the formation process of $Zn_5(OH)_8(NO_3)_2\cdot 2H_2O$ thin films was discussed in detail.

Experimental

Compact large area $Zn_5(OH)_8(NO_3)_2\cdot 2H_2O$, $Co_5(OH)_8(NO_3)_2\cdot 2H_2O$ and Co-doped $Zn_5(OH)_8(NO_3)_2\cdot 2H_2O$ thin films were grown under a bovine serum albumin (BSA) Langmuir monolayer template at room temperature, and NH_3 was used as a catalyst in the kinetically controlled vapor diffusion process. All chemicals used were of analytical grade and used as received. The water used was initially triply distilled and subsequently purified using a Millipore Milli-Q system fitted with a 0.22 μm filter at the outlet.

Langmuir monolayer experiments were performed using a KSV 5000 LB trough (KSV, Finland) enclosed in a cabinet to avoid dust deposition. Zinc nitrate hexahydrate ($Zn(NO_3)_2\cdot 6H_2O$) and cobalt nitrate dihydrate ($Co(NO_3)_2\cdot 2H_2O$) aqueous solutions (0.03 M) and a mixed aqueous solution (0.03 M) containing $Zn^{2+}/Co^{2+} = 9{:}1$ were used as the subphases. BSA solution was prepared according to the method of Sánchez-González *et al.*,[23] 0.05% (v/v) of amyl alcohol was added to improve the spreading process. The pH of the BSA solution was *ca.* 6.3 and that of $Zn(NO_3)_2$ solution was *ca.* 5.7. A 7 μL aqueous solution of BSA with a concentration of 0.1 mM was carefully spread onto the surface of the subphase, and left for 30 min prior to compression. One beaker containing 1800 mL dilute solution of commercial 28% ammonia (diluted with water 1:1000 v/v) was placed in the enclosed cabinet at the beginning of compressing the monolayers to permit ammonia diffusion to the interface. The monolayers were compressed at a compression rate of 3 mm min^{-1} with a target surface pressure of 15 mN m^{-1}, the surface pressure was kept constant at 15 mN m^{-1} after reaching it.

The whole setup was left unstirred until the samples were picked up from the system. Samples of the thin films were prepared for TEM by inserting copper TEM grids through the monolayer and then lifting the grids horizontally from below the monolayer when the surface pressure was stable at 15mN m^{-1} for 20 min or 2 h. The prepared specimens were characterized by electron diffraction (ED) and TEM in the bright-field mode using a JEOL 100CX transmission electron microscope operating at 100 kV.

Samples were similarly prepared for XRD, SEM and XPS by transferring the films formed at the gas–liquid interface onto a glass slide by the horizontal lifting method with a dipping speed of 8 mm min^{-1} when the surface pressure was stable at 15 mN m^{-1} for 2 h. The thin films were air-dried and then characterized.

In order to investigate the effect of organic matrix template on the crystal growth, the products formed at 20 min and 2 h under a BSA Langmuir monolayer in the absence of ammonia were also picked up and characterized by SEM and TEM. These experiments were performed following the procedure described above but in the absence of ammonia diffusion.

Surface features of products were imaged by SEM with a JEOL JSM-5600LV; specimens were mounted on conductive carbon adhesive tabs and examined at 20 kV after gold sputter coating. The crystallinity was characterized by XRD with a Philips, X' Pert Pro MPD using Cu Kα radiation (λ = 1.5406 Å) by the θ/2θ scanning mode. To identify elemental compositions, XPS analysis was performed with a Kratos Axis Ultra system using monochromatic Al Kα X-rays (1486.6 eV) operated at 150 W and 15 kV at a background pressure of approximately 5.0×10^{-9} Torr. A survey spot size and 40 eV pass energy were used for the analysis. Charge neutraliser was used and all the binding energies were calibrated with respect to the hydrocarbon C1s peak at 284.8 eV.

The surface pressure–area (π–A) isotherms of BSA on pure water subphase, zinc nitrate hexahydrate solution subphase in the presence or absence of ammonia diffusion were recorded to monitor the film formation process.

Results and discussion

Metal hydroxide nitrates and doped thin films from aqueous $Zn(NO_3)_2$, $Co(NO_3)_2$ and mixed solutions were prepared by the combination approach of the vapor–liquid interface nucleation template generated by the vapor diffusion of catalyst (ammonia) and the organic matrix template (BSA Langmuir monolayer). Notably, the area of continuous films grown by this method depends on the area of the trough used. In this study the largest area of continuous film was up to 100 cm^2. Moreover, the thin films at the gas–liquid interface are flexible and continuous, which results from the synergetic effect of the dual template.

The effect of each template and the interaction between the template and subphase ions can be demonstrated by the difference of the π–A isotherms. Fig. 1 shows the π–A isotherms of BSA molecules spreading on the subphase of Zn^{2+} solution surface in the presence (Fig. 1a) and absence (Fig. 1b) of ammonia diffusion, and on an ultrapure water surface (Fig. 1c). Surface pressure varies not only with the variation of subphase,

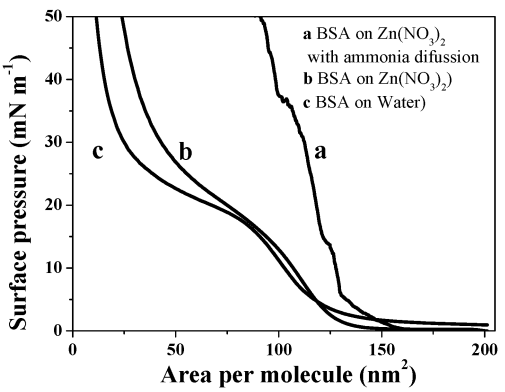

Fig. 1 π–A isotherms of BSA Langmuir monolayer obtained on the subphases of 0.03 M Zn^{2+} solution in the presence (a) and absence (b) of ammonia diffusion in the chamber, and ultrapure water (c) at 23 °C.

but also is related to the presence or absence of ammonia diffusion in the system. As shown in Fig. 1b and c, although the lift-off area (142.0 nm^2 $molecule^{-1}$) of BSA molecules on the Zn^{2+} ion solution surface and the ultrapure water surface are almost the same at the initial stage of monolayer compression, their final limiting areas are different. Specifically, when BSA molecules are spread on the surface of the Zn^{2+} ion subphase, the limiting area is about 53.3 nm^2 $molecule^{-1}$; when they are spread on the ultrapure water surface, the limiting area is only 28.4 nm^2 $molecule^{-1}$. The reason that the lift-off areas of BSA molecules on both surfaces are almost the same at the initial stage is that the electrostatic interactions between BSA molecules and Zn^{2+} ions are not so strong and BSA molecules at the interface are still in the gas phase at this stage, so the surface pressure is not sensitive to the change of individual BSA molecules generated by the electrostatic interactions. However, as compression increases and time increases, more and more Zn^{2+} ions are enriched to the interface and gradually combined with BSA molecules by the electrostatic interactions, leading to increasing volume of BSA molecules and promoting the phase transmission of the monolayer; as a result, the final limiting area on the Zn^{2+} ion solution surface is much larger than that on the ultrapure water surface.[24]

As shown in Fig. 1a, when the ammonia is diffused to the Zn^{2+} ion solution surface, $NH_3 \cdot H_2O$ is firstly formed by combination of ammonia vapor with water at the gas–liquid interface, then OH^- anions are generated by hydrolysis of $NH_3 \cdot H_2O$ at the vapor–liquid interface. Thus, a pH-gradient is established at the interface as the ammonia diffusion continues.[22] The negative charge density at the interface increases, resulting in increasing of the electrostatic interactions between Zn^{2+} ions and both organic template and vapor–liquid interface. More importantly, the vapor–liquid interface as a nucleation template provides more nucleation sites for Zn^{2+} ions. Therefore, more Zn^{2+} ions are enriched to the vapor–liquid interface, which makes more crystals form faster than the case in the absence of the diffusion of ammonia. As a result, the initial lift-off area (Fig. 1a) has a small increase to 159.2 nm^2 $molecule^{-1}$ and the final limiting area reaches 115.3 nm^2 $molecule^{-1}$. The shaking of the π–A isotherm is due to the instability of the surface tension caused by the fast formation of crystal thin films, and the diffusion of ammonia at the interface as well. It is the presence of the organic matrix template and the vapor–liquid interface nucleation template that allows the control of the nucleation and the growth of crystals at the interface, and they both influence the growth of crystals and the formation of the thin films.

Firstly, the effect of organic matrix template on the crystal growth was investigated. Fig. 2a shows the TEM image of crystals formed under the BSA Langmuir monolayer template at the surface pressure of 15 mN m^{-1} for 20 min. Individual nanosheet crystals can be observed in Fig. 2a, some crystals stand while some lie, which is further confirmed by SEM images (Fig. 2c–d). Their lengths and widths are *ca.* 1–2 μm and *ca.* 100–200 nm, respectively. The selected area electron diffraction (SAED) pattern (Fig. 2b), recorded on the rectangular area shown in Fig. 2a, shows 6-fold symmetry and confirms that the nanosheets are highly ordered single crystal structures. Such structure features are kept and seen more clearly as the growth time increases. Fig. 3 presents the TEM image and SEM

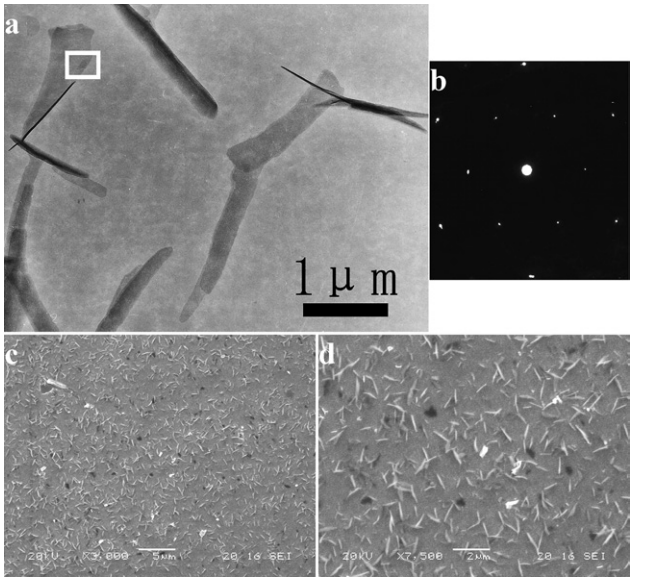

Fig. 2 TEM image (a), SAED pattern (b), and SEM images (c and d) of the nanosheets grown under only the BSA Langmuir monolayer for 20 min at a surface pressure of 15 mN m^{-1}. Scale bars in a: 1 μm, c: 5 μm and d: 2 μm.

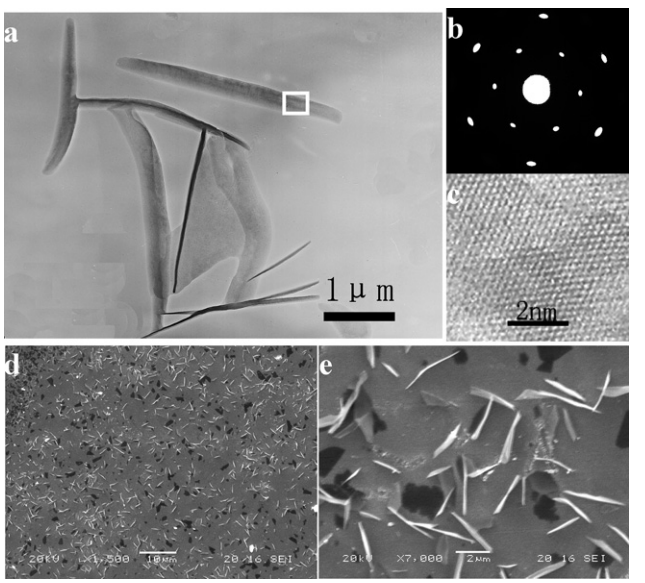

Fig. 3 TEM image (a), SAED pattern (b), HR-TEM image (c), and SEM images (d and e) of the nanosheets grown under the BSA Langmuir monolayer for 2 h at a surface pressure of 15 mN m^{-1}. Scale bars in a: 1 μm, c: 2 nm, d: 10 μm and d: 2 μm.

images of crystals formed at 2 h under the BSA Langmuir monolayer template. The TEM image in Fig. 3a exhibits the same morphology and structure as Fig. 2a, but the crystals are larger than those at 20 min. A high-resolution TEM image (HR-TEM) shown in Fig. 3c presents good crystallinity, and clear well-defined lattice fingers are in good agreement with the SAED pattern taken on the same area shown in Fig. 3b. Fig. 3d–e show the SEM images of the products at different magnifications; large area nanosheets are uniformly distributed and some

crystals stand while some lie, which is consistent with Fig. 2c–d. As discussed above, the growing time only influences the sizes of nanosheet crystals, rather than their morphologies and structures.

It is remarkable that an interesting phenomenon was identified in a recent publication:[25] Casse *et al.* found that even a rather flexible matrix like a block copolymer film at the air–water interface not only leads to uniform particles with identical particle sizes, but also can act as a tool for the 2D arrangement of the resulting particles in a near-crystalline order in a distorted hexagonal lattice.[25] Regulation of mineralization on the atomic (crystal phase) and the nanoscopic (particle size and shape) scale in the reported work is often encountered in cases where inorganic crystals are mineralized under organic matrix templates. Those mineralized inorganic crystals usually adopt a preferred orientation along a specific plane, even a single crystal structure at the atomic scale, while they display a uniform particle size and shape at the nanoscopic scale, just like the results shown in Fig. 3. However, it is seldom observed for the 2D arrangement of the resulting particles in a near-crystalline order. The main reason for the phenomenon is perhaps due to a special stage of balance between the nucleation and the growth of calcium phosphate at a very low concentration and a suitable pH value of the subphase; such conditions make the nucleation and growth process of minerals well defined. In our recent work, we have also found that our dual template approach can lead to a 2D aggregation of crystals with a special fractal structure, and we will discuss and compare them in detail in another paper. Both Casse's work[25] and our work give an implication that the organic matrix templates can realize effective control of the mineralization of inorganic crystals, which provides us a good model for biological mineralization and an opportunity to obtain a series of inorganic materials with special structure features.

However, when the vapor–liquid interface template generated by the kinetically controlled vapor diffusion of ammonia exists together with the organic matrix template on the surface of the subphase, it is notably different from the situation when only the organic matrix template is present. The TEM and HR-TEM images of $Zn_5(OH)_8(NO_3)_2\cdot 2H_2O$ films formed at 20 min under the BSA Langmuir monolayer at a surface pressure of 15 mN m^{-1} in the presence of ammonia diffusion are shown in Fig. 4. Compared with Fig. 2a, Fig. 4a shows a continuous films rather than the individual nanosheets in the presence of ammonia. It is obvious that the vapor–liquid interface template generated by the kinetically controlled vapor diffusion of ammonia plays a key role in the formation of the thin films. The diffusion through a solution of molecular precursor $[Zn(NO_3)_2\cdot 6H_2O]$ establishes a spatially and temporally regulated gradient of the catalyst (ammonia), to control the supersaturation of $Zn_5(OH)_8(NO_3)_2\cdot 2H_2O$ through the formation of complexes,[26] while the vapor–liquid interface serves as the nucleation template.[21] Such a template as assistant of the BSA organic template directs crystal growth where there are no nanosheets induced by the BSA Langmuir monolayer (like the blank areas in Fig. 2a). The co-operation effect between the vapor–liquid interface template and the organic template directs the growing materials to adopt a continuous film morphology; in contrast, the competition effect between the two templates leads to the morphological differences between nanosheets in the films and those as shown in Fig. 2a.

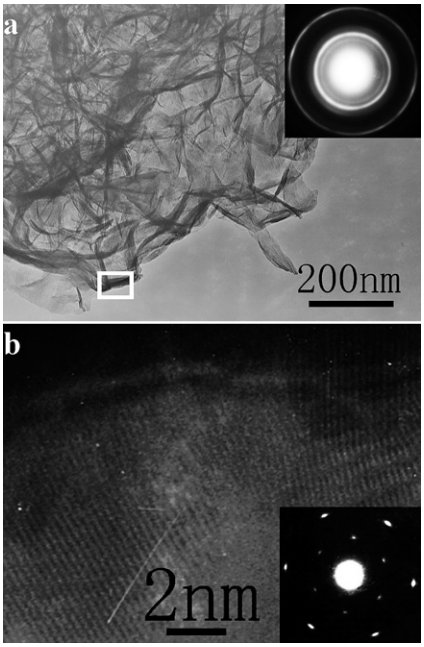

Fig. 4 TEM image (a) and ED pattern (inset), HR-TEM image (b) and SAED pattern (inset) of the thin films formed under the BSA Langmuir monolayer in the presence of ammonia for 20 min at a surface pressure of 15 mN m^{-1}. Scale bars in a: 200 nm and b: 2 nm.

The inset in Fig. 4a is the ED pattern of the film, indicating a polycrystalline structure. Fig. 4b is the HR-TEM image recorded at the rectangular area shown in Fig. 4a and shows the same structure as Fig. 3c. The inset in Fig. 4b is the SAED pattern recorded at the same area, showing the same structural features as Fig. 2b and Fig. 3b. By comparison of Fig. 2 and Fig. 4, it is easy to see that the organic template favors the formation of individual single-crystal nanosheets whereas the dual template is propitious to the construction of continuous polycrystalline films, but there exist still some single-crystal domains in polycrystalline films. This observation confirms that co-operation and competition (synergetic effect) of the dual template at the interface lead to the structure containing single-crystal domains in the polycrystalline films.

TEM images of films formed at 2 h under the BSA Langmuir monolayer template in the presence of ammonia diffusion are shown in Fig. 5. It can be seen in Fig. 5a, c and e, the films of $Zn_5(OH)_8(NO_3)_2\cdot 2H_2O$, $Co_5(OH)_8(NO_3)_2\cdot 2H_2O$ and Co-doped $Zn_5(OH)_8(NO_3)_2\cdot 2H_2O$ with similar morphologies and structures to those observed in Fig. 4a are formed. Fig. 5b, d and f are the high-magnification images of Fig. 5a, c and e. It is obvious that the films are continuous and compact. The films of $Zn_5(OH)_8(NO_3)_2\cdot 2H_2O$ in Fig. 5a are more compact than those in Fig. 4a formed at 20 min, but they show similar inner structure features. The corresponding ED patterns (insets in Fig. 5b, d and f) show a polycrystalline structure of the films just like the films in Fig. 4a formed at 20 min. As discussed above, more growing time only makes the thin films more compact, rather than changing their inner structures.

Surface morphologies of the films formed at 2 h were also examined using SEM. The SEM images of $Zn_5(OH)_8(NO_3)_2\cdot 2H_2O$ (Fig. 6a, b and c), $Co_5(OH)_8(NO_3)_2\cdot 2H_2O$

(Fig 6d, e and f), and Co-doped $Zn_5(OH)_8(NO_3)_2\cdot 2H_2O$ (Fig 6g, h and i) films are shown in Fig. 6. As shown in Fig. 6a, d and g, large area films of $Zn_5(OH)_8(NO_3)_2\cdot 2H_2O$, $Co_5(OH)_8(NO_3)_2\cdot 2H_2O$ and Co-doped $Zn_5(OH)_8(NO_3)_2\cdot 2H_2O$ possess uniform and smooth surface morphologies, and there are no cracks in the films. Fig. 6b, e and h are the high-magnification images of Fig. 6a, d and g. The high-magnification images show that the films are continuous and compact. The side view SEM images of the films are shown in Fig. 6c, f and i, indicating that the thicknesses of $Zn_5(OH)_8(NO_3)_2\cdot 2H_2O$ and Co-doped $Zn_5(OH)_8(NO_3)_2\cdot 2H_2O$ thin films are *ca.* 1.2 μm and the thickness of $Co_5(OH)_8(NO_3)_2\cdot 2H_2O$ thin films is *ca.* 2 μm, respectively.

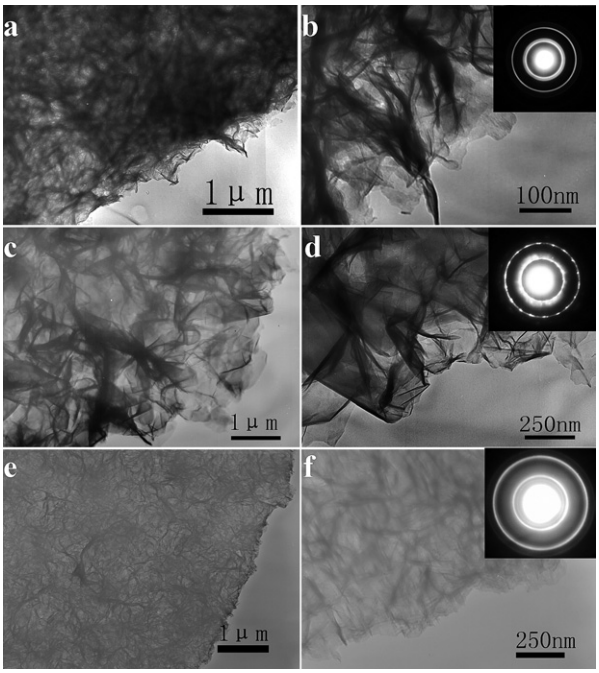

Fig. 5 TEM images of $Zn_5(OH)_8(NO_3)_2\cdot 2H_2O$ (a and b), $Co_5(OH)_8(NO_3)_2\cdot 2H_2O$ (c and d) and Co-doped $Zn_5(OH)_8(NO_3)_2\cdot 2H_2O$ thin films (e and f) formed at 2 h in the presence of dual template. Scale bars are 1 μm in a, c and e, 100 nm in b, 250 nm in d and f. Insets in b, d and f are the corresponding ED patterns.

The XRD patterns of the thin films formed under BSA Langmuir monolayers at a surface pressure of 15 mN m^{-1} at 2 h on the surfaces of Co^{2+} solution (a), Zn^{2+} solution (b) and Zn^{2+}/Co^{2+} mixed solution (c) in the presence of ammonia diffusion are shown in Fig. 7. The peak at 9.442° in Fig. 7a corresponds to the (200) face of $Co_5(OH)_8(NO_3)_2\cdot 2H_2O$.[21,27] The strong peak at 9.087° and the relatively weak peak at 18.232° in Fig. 7b are assigned to the (200) and (400) faces of $Zn_5(OH)_8(NO_3)_2\cdot 2H_2O$, respectively.[28] The XRD pattern of Co doped $Zn_5(OH)_8(NO_3)_2\cdot 2H_2O$ is shown in Fig. 7c, the two peaks at 9.168° and 18.319° are slightly shifted compared to the (200) and (400) peaks of $Zn_5(OH)_8(NO_3)_2\cdot 2H_2O$, which not only indicates that Co-doped $Zn_5(OH)_8(NO_3)_2\cdot 2H_2O$ films retain the same crystal structure as the undoped $Zn_5(OH)_8(NO_3)_2\cdot 2H_2O$ films, but also suggests that Zn^{2+} ions in the lattices of $Zn_5(OH)_8(NO_3)_2\cdot 2H_2O$ have been partially substituted by Co^{2+} ions.[29] The ionic radii of Co^{2+} and Zn^{2+} ions are 0.72 Å and 0.74 Å, respectively.[30] When Co^{2+} ions partially substitute for Zn^{2+} ions, the interlayer spacing of (200) plane becomes a little smaller because of the smaller size of the Co^{2+} ion than the Zn^{2+} ion. In addition, the diffraction peak of the (400) plane is the second-order diffraction peak of the (200) plane, indicating that the thin films are well-orientated. Comparisons of preferred orientation XRD patterns and

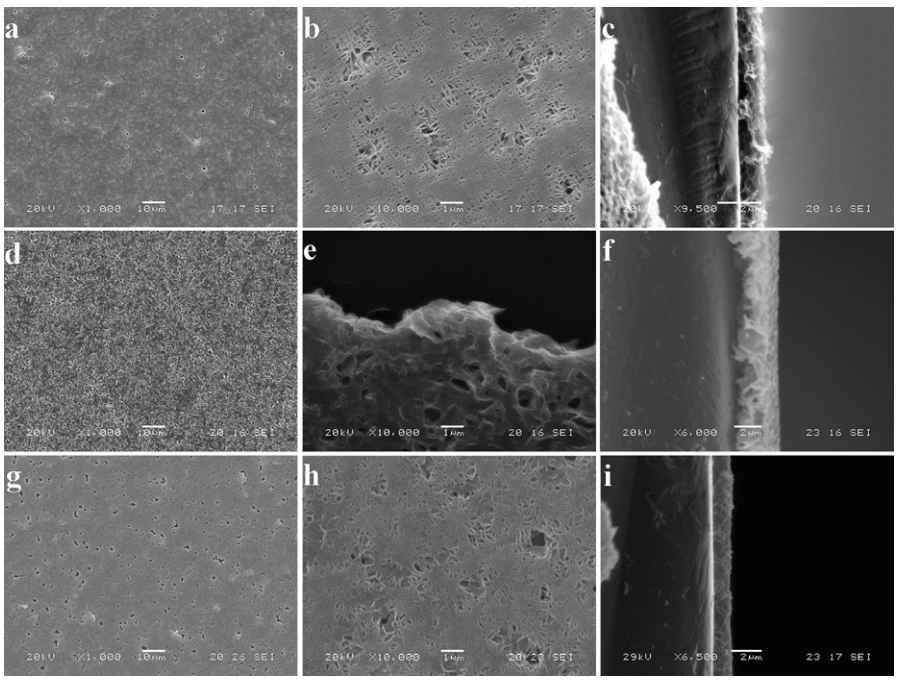

Fig. 6 The SEM images of the films obtained at 2 h in the presence of dual template: top views at different magnifications of $Zn_5(OH)_8(NO_3)_2\cdot 2H_2O$ (a and b), $Co_5(OH)_8(NO_3)_2\cdot 2H_2O$ (d and e), and Co-doped $Zn_5(OH)_8(NO_3)_2\cdot 2H_2O$ thin films (g and h); side view of $Zn_5(OH)_8(NO_3)_2\cdot 2H_2O$ (c), $Co_5(OH)_8(NO_3)_2\cdot 2H_2O$ (f), and Co-doped $Zn_5(OH)_8(NO_3)_2\cdot 2H_2O$ thin films (i). Scale bars are 10 μm in a, d, g; 1 μm in b, e, h; and 2 μm in c, f, i.

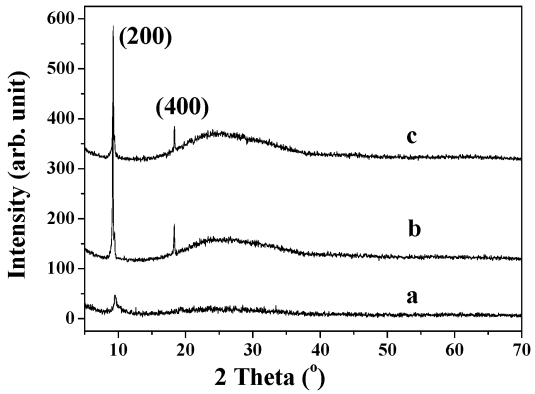

Fig. 7 XRD patterns of the films formed under BSA Langmuir monolayer at a surface pressure of 15 mN m^{-1} at 2 h on the surfaces of 0.03 M Co^{2+} solution (a), 0.03 M Zn^{2+} solution (b) and 0.03 M Zn^{2+}/Co^{2+} mixed solution (c) in the presence of ammonia diffusion.

polycrystalline ED patterns (see insets of Fig. 5b, d and f) suggest that each layer of the crystal faces along the (200) plane is in alignment with neighboring layers,[31,32] and the layers are parallel and equidistant but rotate with respect to each other.[21,33]

Here, the uniform surface morphologies and the preferred orientation along (200) plane of the films are ascribed to the special structural features of the materials and the synergetic effect of the dual template in our research system. $Zn_5(OH)_8(NO_3)_2\cdot 2H_2O$, as we know, consists of layered sheets with octahedrally coordinated Zn^{2+} ions in the brucite layer, one quarter of which are replaced by two tetrahedrally coordinated Zn^{2+} ions located above and below the plane of the octahedrally coordinated Zn^{2+} ions.[12,28] The nitrate anions are located between the sheets and do not directly coordinate to the zinc atoms. There are only zinc atoms in the (200) plane, which indicates that the (200) plane is a polar plane. When BSA molecules are spread on the surface of $Zn(NO_3)_2$ solution, the Zn^{2+} ions are strongly attracted by the negative charge of BSA Langmuir monolayers through electrostatic interactions, therefore, the nucleation along the (200) plane is facilitated because of the strong polarity of the (200) plane. Furthermore, it has been proposed that structural flexibility in the organic monolayer plays an important role in the orientated growth of inorganic crystals.[34] A cooperative interaction between the organic templates and inorganic phases leads to local re-arrangement of the Langmuir films during the nucleation stage.[34] Here, the interactions between the BSA molecules and Zn^{2+} ions in the subphase solution make the monolayer self-regulate its structure in the formation of the inorganic crystals; at the same time, the formation of inorganic crystals is also influenced by the self-regulation of the monolayer, which should be a synergetic process of adapting each other and adjusting each other. What is most important is that the structural flexibility of the BSA monolayer provides a means for the regulation and adjustment. All of these factors above lead to the decrease of the interfacial energy and improve the preferred orientation along the (200) plane. For $Co_5(OH)_8(NO_3)_2\cdot 2H_2O$ and Co-doped $Zn_5(OH)_8(NO_3)_2\cdot 2H_2O$, a similar situation takes place.

The surface compositions of $Zn_5(OH)_8(NO_3)_2\cdot 2H_2O$, $Co_5(OH)_8(NO_3)_2\cdot 2H_2O$ and Co-doped $Zn_5(OH)_8(NO_3)_2\cdot 2H_2O$ thin films were analyzed using X-ray photoelectron spectroscopy. The high resolution XPS spectra of Zn 2p, Co 2p and N 1s of the thin films are shown in Fig. 8. Peaks at 1021.7 eV and weaker peaks at 1044.9 eV shown in Fig. 8a are assigned to Zn $2p_{3/2}$ and Zn $2p_{1/2}$ in $Zn_5(OH)_8(NO_3)_2\cdot 2H_2O$ (I) and Co-doped $Zn_5(OH)_8(NO_3)_2\cdot 2H_2O$ (II) respectively. The high resolution XPS spectra of Co 2p are shown in Fig. 8b: Co $2p_{3/2}$ and Co $2p_{1/2}$ are centered at 780.8 eV and 796.7 eV respectively in $Co_5(OH)_8(NO_3)_2\cdot 2H_2O$ (I) and Co-doped $Zn_5(OH)_8(NO_3)_2\cdot 2H_2O$ (II), which is in agreement with the report of Morse *et al.*,[21] and the two peaks at higher binding energy are attributed to the shake-up satellites of Co^{2+}. The occurrence of the Co 2p signal unambiguously confirms the existence of Co^{2+} in the doped films, being consistent with the result of XRD. The N 1s peaks of the thin films centered at 400.0 eV, as shown in Fig. 8c I, II and III, are assigned to the N 1s of BSA molecules,[35] and the

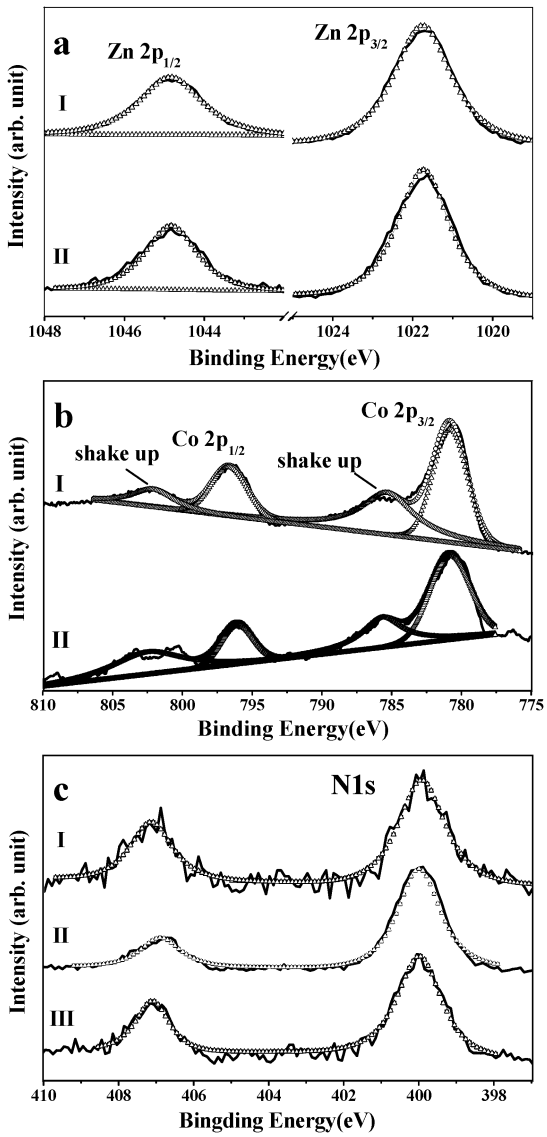

Fig. 8 High resolution XPS spectra of a: Zn 2p region of $Zn_5(OH)_8(NO_3)_2\cdot 2H_2O$ (I) and Co-doped $Zn_5(OH)_8(NO_3)_2\cdot 2H_2O$ (II); b: Co 2p region of $Co_5(OH)_8(NO_3)_2\cdot 2H_2O$ (I) and Co-doped $Zn_5(OH)_8(NO_3)_2\cdot 2H_2O$ (II); c: N 1s region of $Zn_5(OH)_8(NO_3)_2\cdot 2H_2O$ (I), $Co_5(OH)_8(NO_3)_2\cdot 2H_2O$ (II) and Co-doped $Zn_5(OH)_8(NO_3)_2\cdot 2H_2O$ (III).

N 1s peaks centered at 407.1 eV in I, III and 406.9 eV in II correspond to the report on the nitrates.[36] Such slight differences of the N 1s peaks of the nitrates are due to the chemical environment difference of Co and Zn in the materials. The atomic concentration of Co in Co-doped films is about 1.5%. The results of XPS analysis confirm that the Co-doped $Zn_5(OH)_8(NO_3)_2 \cdot 2H_2O$ thin films are successfully fabricated.

Conclusions

In summary, we developed a combination strategy of the vapor–liquid interface nucleation template and the organic substrate template, thus, compact large-area $Zn_5(OH)_8(NO_3)_2 \cdot 2H_2O$, $Co_5(OH)_8(NO_3)_2 \cdot 2H_2O$, and Co-doped $Zn_5(OH)_8(NO_3)_2 \cdot 2H_2O$ thin films with uniform surface morphology and good orientation were synthesized at ambient temperature. Such a dual-template approach captures the advantages of both the vapor–liquid interface generated by the vapor diffusion of catalyst (ammonia) which served as one nucleation template providing kinetic control and the crystal growth regulated by the organic matrix template providing control of crystal structures and morphologies.[37–39] Provided that controls of the concentration of subphase, the velocity of ammonia diffusion and the surface pressure of monolayer are appropriate, such a dual-template biomimetic approach provides an opportunity for preparing large area well-oriented materials with special morphologies and structural features at room temperature.

Acknowledgements

This work was financially supported by National Natural Science Foundation of China (No. 20371015 and 10874040), State Key Basic Research "973" Plan of China (No. 2007CB616911) and the Cultivation Fund of the Key Scientific and Technical Innovation Project, Ministry of Education of China (No. 708062).

References

1 K. Naka and Y. Chujo, *Chem. Mater.*, 2001, **13**, 3245.
2 T. Kato, A. Sugawara and N. Hosoda, *Adv. Mater.*, 2002, **14**, 869.
3 H. Cölfen and S. Mann, *Angew. Chem. Int. Ed.*, 2003, **42**, 2350.
4 C. B. Mao, D. J. Solis, B. D. Reiss, S. T. Kottmann, R. Y. Sweeney, A. Hayhurst, G. Georgiou, B. Iverson and A. M. Belcher, *Science*, 2004, **303**, 213.
5 J. P. Yang, F. C. Meldrum and J. H. Fendler, *J. Phys. Chem.*, 1995, **99**, 5500.
6 S. Mann, B. R. Heywood, S. Rajam and J. D. Birchall, *Nature*, 1988, **334**, 692.
7 E. DiMasi, *Langmuir*, 2002, **18**, 8902.
8 H. Wakayama, S. R. Hall and S. Mann, *J. Mater. Chem.*, 2005, **15**, 1134.
9 M. J. Olszta, S. Gajjeraman, M. Kaufman and L. B. Gower, *Chem. Mater.*, 2004, **16**, 2355.
10 J. M. Ouyang and S. P. Deng, *Dalton Trans.*, 2003, 2846.
11 S. H. Yu, H. Cölfen, A. W. Xu and W. F. Dong, *Cryst. Growth Des.*, 2004, **4**, 33.
12 T. Biswick, W. Jones, A. Pacu, E. Serwick and J. Podobinski, *J. Solid State Chem.*, 2007, **180**, 1171.
13 G. P. Gillman, M. A. Noblea and M. D. Raven, *Applied Clay Science*, 2008, **38**, 179.
14 Z. L. Wang, E. B. Wang, L. Gao and L. Xu, *J. Solid State Chem.*, 2005, **178**, 736.
15 S. Gago, M. Pillinger, T. Santos, J. Rocha and I. Gonçalves, *Eur. J. Inorg. Chem.*, 2004, **7**, 1357.
16 S. Gago, M. Pillinger, T. Santos, J. Rocha and I. Gonçalves, *Eur. J. Inorg. Chem.*, 2004, **7**, 1389.
17 M. D. Arco, S. Gutiérrez, C. Martín, V. Rives and J. Rocha, *J. Solid State Chem.*, 2004, **177**, 3954.
18 C. L. Zhu, C. N. Chen, L. Y. Hao, Y. Hu and Z. Y. Chen, *J. Cryst. Growth*, 2004, **263**, 473.
19 K. Kakiuchi, E. Hosono, Toshio Kimura, H. Imai and S. Fujihara, *J. Sol-Gel Sci. Tech.*, 2006, **39**, 63.
20 E. Hosono, S. Fujihara and T. Kimura, *J. Mater. Chem.*, 2004, **14**, 881.
21 B. Schwenzer, K. M. Roth, J. R. Gomm, M. Murr and D. E. Morse, *J. Mater. Chem.*, 2006, **16**, 401.
22 D. Kisailus, B. Schwenzer, J. Comm, J. C. Weaver and D. E. Morse, *J. Am. Chem. Soc.*, 2006, **128**, 10276.
23 J. Sánchez-González, J. Ruiz-García and M. J. Gálvez-Ruiz, *J. Colloid Interface Sci.*, 2003, **267**, 286.
24 G. K. Chudinova, O. N. Pokrovskaya and A. P. Savitskii, *Russ. Chem. Bull.*, 1995, **44**, 1958.
25 O. Casse, O. Colombani, K. Kita-Tokarczyk, A. H. E. Müller, W. Meier and A. Taubert, *Faraday Discuss.*, 2008, **139**, 179.
26 B. Schwenzer, John R. Gomm and D. E. Morse, *Langmuir*, 2006, **22**, 9829.
27 M. Kurmoo, *Chem. Mater.*, 1999, **11**, 3370.
28 W. Stählin and H. R. Oswald, *Acta Crystallogr., Sect. B.*, 1970, **26**, 860.
29 A. S. Risbud, N. A. Spaldin, Z. Q. Chen, S. Stemmer and R. Seshadri, *Phys. Rev. B*, 2003, **68**, 205202.
30 R. D. Shannon, *Acta Cryst., Sec. A*, 1976, **32**, 751.
31 R. S. Jayashree and P. V. Kamath, *J. Mater. Chem.*, 1999, **9**, 961.
32 K. T. Ehlsissen, A. Delahaye-Vidal, P. Genin, M. Figlarz and P. Wiliams, *J. Mater. Chem.*, 1993, **3**, 883.
33 B. D. Cullity, *Elements of X-Ray Diffraction*, 2nd edn, Addison-Wesley, Reading, MA, 1978.
34 S. J. Cooper, R. B. Sessions and S. D. Lubetkin, *J. Am. Chem. Soc.*, 1998, **120**, 2090.
35 Y. F. Dufrêne, T. G. Marchal and P. G. Rouxhet, *Appl. Surf. Sci.*, 1999, **144–145**, 638.
36 J. F. Moulder, W. F. Stickle, P. E. Sobol, and K. D. Bomben, *Handbook of X-ray Photoelectron Spectroscopy*, ed. J. Chastain and R. C. King, Physical Electronics, Eden Praire, MN, 1995.
37 J. L. Sumerel, W. Yang, D. Kisailus, J. C. Weaver, J. H. Choi and D. E. Morse, *Chem. Mater.*, 2003, **15**, 4804.
38 D. Kisailus, J. H. Choi, J. C. Weaver, W. Yang and D. E. Morse, *Adv. Mater.*, 2005, **17**, 314.
39 E. Hosono, S. Fujihara, I. Honma and H. Zhou, *J. Mater. Chem.*, 2005, **15**, 1938.